Physics of Plasmas ARTICLE scitation.org/journal/php

Global gyrokinetic simulation of microturbulence with kinetic electrons in the presence of magnetic island in tokamak

Cite as: Phys. Plasmas **26**, 052510 (2019); doi: 10.1063/1.5096962
Submitted: 21 March 2019 · Accepted: 30 April 2019 ·
Published Online: 20 May 2019

K. S. Fang[1] and Z. Lin[2,a)]

AFFILIATIONS

[1]Fusion Simulation Center and State Key Laboratory of Nuclear Physics and Technology, Peking University, Beijing 100871, People's Republic of China
[2]Department of Physics and Astronomy, University of California, Irvine, California 92697, USA

[a)]Electronic mail: zhihongl@uci.edu

ABSTRACT

An electrostatic model has been formulated and implemented in the gyrokinetic toroidal code to study the nonlinear ion temperature gradient (ITG) turbulence in the presence of an $n = 1$, $m = 2$ magnetic island. The ions are described by the gyrokinetic equation while the electrons are treated with the drift-kinetic equation. In our simulation, an $n = 1$, $m = 2$ electrostatic mode is formed with the same vortex structure of the magnetic island. When the magnetic island flattening effect is turned on, the island vortex mode is well preserved and couples to the $n = 0$, $m = 0$ geodesic acoustic mode. Simulation shows that the magnetic island can suppress the ITG turbulence at the island O-point and strengthen it near the X-point. We show that the vortex mode can generate a substantial helical shear flow around the island. We also find that the turbulence and transport are suppressed inside the island and enhanced at the island X-point.

I. INTRODUCTION

Magnetic islands in toroidally confined plasmas can be generated externally by resonant magnetic perturbations (RMPs)[1,2] or internally by magnetohydrodynamic (MHD) instabilities such as tearing modes or neoclassical tearing modes.[3,4] Magnetic islands can flatten the local pressure profile and modify plasma flow, thus affecting microturbulence and neoclassical bootstrap current.[5] On the other hand, microturbulence regulates plasma current and electron heat conductivity along and across the magnetic field lines, thus affecting island dynamics. The effects of magnetic islands on plasma confinement are not well understood. For example, an outstanding issue is the role of low order rational surface in the formation of internal transport barriers (ITBs).[6] A speculation is that resistive MHD instabilities (tearing modes) produce magnetic islands and drive strong sheared flows around the low order rational surface, which suppress the turbulent transport. Another example is the role of magnetic islands in the density pump out and suppression of the edge localized mode by RMP.[1]

To address these questions, a thorough understanding of the magnetic island effects on microturbulence is needed. Recently, progress has been made.[7–16] Both theoretical analysis and global gyrokinetic simulations[7,8] find that magnetic islands can modify the structures of the ion temperature gradient mode (ITG)[17,18] due to the flattening effect. Gyrofluid simulations[9–11] find that large magnetic islands can produce a broad distribution of rational surfaces near the O-point, leading to both radial and poloidal mode coupling and form a global-type ITG eigenmode. Flux-tube continuum and global fluid simulations[12–14] reveal that the ITG turbulence can generate an electrostatic vortex mode with the same structure as the island topology, which induces strong $E \times B$ shear flows around the island separatrix. Both global particle and local continuum simulations[15,16] find that the island induced shear flows significantly suppress the microturbulence. These studies have illustrated some important features of the magnetic island effects on microturbulence. However, most of previous simulations are based on reduced models such as local geometry, adiabatic electrons, or fluid models. Global kinetic simulation is needed for cross-scale coupling with the wave-particle interaction treated on the same footings. In particular, electron dynamics is critical for driving the trapped electron mode turbulence and for generating bootstrap current responsible for the neoclassical tearing mode.

In this work, a global particle-in-cell (PIC) simulation model with the magnetic island is formulated and then implemented in the 3D gyrokinetic toroidal code (GTC).[19,20] We solve the dynamics of gyrokinetic ions and drift-kinetic electrons (DKEs) in a full torus tokamak configuration. Based on the time scale separation between microturbulence and magnetic island, the island is prescribed, and for

simplicity, it is assumed to be static without rotation.[21] To investigate the ITG in the presence of the magnetic island, a prescribed n = 1, m = 2 magnetic island is added in the system. First, we demonstrate that by only keeping the island effects in the particle $E \times B$ drift and the parallel motion terms but ignoring the island's flattening effect, an n = 1, m = 2 electrostatic vortex mode with the same structure as the island (i.e., the zonal mode on the island flux surface) can be excited in the nonlinear stage. To further study the island effect on the ITG turbulence, we turn on the flattening effect and allow the system to evolve to a flattened state as the initial condition for the self-consistent simulation. We find that with the flattening effect, the n = 1, m = 2 island vortex mode structure is well preserved. More interestingly, the mode is also coupled with the n = 0, m = 0 mode to synchronously oscillate with the geodesic acoustic mode (GAM)[22,23] frequency. Furthermore, the magnetic island significantly changes the ITG mode structure and regulates the nonlinear ITG turbulence and transport. We have identified that this island vortex mode can generate strong helical shear flow around the island, which can be an important factor of local turbulence suppression. Indeed, the nonlinear ITG fluctuation amplitude peaks near the island's X-point and diminishes around the O-point. Correspondingly, the turbulence intensity is decreased inside the island compared with the no-island case. The particle diffusivities and the heat conductivities of the ions and electrons are also localized at the X-point.

The remainder of this paper is organized as follows: Sec. II describes our simulation model. In Sec. III, we apply an n = 1, m = 2 magnetic island in the model to study the ITG mode, and the magnetic island flattening effect is turned off in this section. Next, in Sec. IV, we turn on the flattening effect to study the ITG under the flattened plasma profile. Section V is a brief conclusion.

II. GYROKINETIC SIMULATION MODEL

GTC uses the gyrokinetic equation to study low frequency plasma physics

$$\frac{d}{dt}f_s(\boldsymbol{R}, v_\parallel, \mu, t) = \left(\frac{\partial}{\partial t} + \dot{\boldsymbol{R}}\cdot\nabla + \dot{v_\parallel}\frac{\partial}{\partial v_\parallel} - C_s\right)f_s = 0. \tag{1}$$

The distribution function $f_s(\boldsymbol{R}, v_\parallel, \mu, t)$ for the species s is described by five dimensional independent variables: the gyrocenter position $\boldsymbol{R}$, the parallel velocity $v_\parallel$, and the magnetic momentum μ. The gyrocenter velocity is denoted by $\dot{\boldsymbol{R}}$; the parallel acceleration is $\dot{v_\parallel}$; and the collision operator is C_s. In this work, we do not take any collision effect into account and simply set $C_s = 0$. In the electrostatic case, the equation for $\dot{\boldsymbol{R}}$ and $\dot{v_\parallel}$ is

$$\dot{\boldsymbol{R}} = v_\parallel\frac{\boldsymbol{B}}{B_\parallel^*} + \boldsymbol{v_E} + \boldsymbol{v_c} + \boldsymbol{v_g}, \tag{2}$$

$$\dot{v_\parallel} = -\frac{1}{m_s}\frac{\boldsymbol{B}^*}{B_\parallel^*}\cdot(\mu\nabla B + Z_s\nabla\delta\phi), \tag{3}$$

where $\boldsymbol{B}, \delta\phi$ are the background magnetic field and the perturbed electrostatic potential, respectively; $\boldsymbol{b} \equiv \frac{\boldsymbol{B}}{B}, \boldsymbol{B}^* = \boldsymbol{B} + \frac{m_s c}{Z_s}v_\parallel\nabla\times\boldsymbol{b}, B_\parallel^* = \boldsymbol{B}^*\cdot\boldsymbol{b}$, respectively; m_s, Z_s, and c denote the particle mass, the electric charge, and the light speed, respectively; $\boldsymbol{v_E} = \frac{c\boldsymbol{b}\times\nabla\delta\phi}{B_\parallel^*}$, $\boldsymbol{v_c} = \frac{m_s c}{Z_s B_\parallel^*}v_\parallel^2\nabla\times\boldsymbol{b}, \boldsymbol{v_g} = \frac{c\mu}{Z_s B_\parallel^*}\boldsymbol{b}\times\nabla B$ are the $E\times B$ drift velocity, the magnetic curvature drift velocity, and the magnetic gradient drift velocity.

When a static island is applied in the system, we treat it as a superposition to the equilibrium magnetic field, namely, $\boldsymbol{B} = \boldsymbol{B_0} + \boldsymbol{\delta B_{IS}}$, where $\boldsymbol{B_0}$ is the equilibrium magnetic field without the magnetic island, and $\boldsymbol{\delta B_{IS}} = \nabla\times(\lambda\boldsymbol{B_0})$ is the island part. Considered that $\boldsymbol{\delta B_{IS}}$ is typically much smaller than B_0 $\left(\frac{\|\boldsymbol{\delta B_{IS}}\|}{\|\boldsymbol{B_0}\|} \sim 10^{-4}\right)$, we can keep $B_\parallel^*$ to the first order with $B_\parallel^* = B_{0\parallel}^* + \delta B_\parallel^*$, where $B_{0\parallel}^* = (\boldsymbol{B_0} + \frac{m_s c}{Z_s}v_\parallel\nabla\times\boldsymbol{b_0})\cdot\boldsymbol{b_0}$ and $\delta B_\parallel^* = 2\boldsymbol{\delta B_{IS}}\cdot\boldsymbol{b_0} + \frac{m_s c}{Z_s}v_\parallel[\nabla\times\left(\frac{\boldsymbol{\delta B_{IS}}}{B_0}\right)\cdot\boldsymbol{b_0} + \nabla\times\boldsymbol{b_0}\cdot\frac{\boldsymbol{\delta B_{IS}}}{B_0}]$. We want to keep the island effects in the $E\times B$ drift, which can be important for the generation of the helical shear flow around the magnetic island. On the other hand, the magnetic island effects in $\boldsymbol{v_c}, \boldsymbol{v_g}$ are ignorable $\left(\frac{\|\boldsymbol{\delta B_{IS}}\|}{\|\boldsymbol{B_0}\|} \sim 10^{-4}\right)$, since it only cause a small perturbation to the particle trajectory. Thus, the following approximations are used:

$$\begin{cases} \boldsymbol{v_E} = \dfrac{c(\boldsymbol{b_0} + \boldsymbol{\delta B_{IS}}/B_0)\times\nabla\delta\phi}{B_\parallel^*}, \\ \boldsymbol{v_c} = \dfrac{m_s c}{Z_s B_\parallel^*}v_\parallel^2\nabla\times\boldsymbol{b_0}, \\ \boldsymbol{v_g} = \dfrac{c\mu}{Z_s B_\parallel^*}\boldsymbol{b_0}\times\nabla B_0, \\ \nabla\times\boldsymbol{b}\cdot\nabla B = \nabla\times\boldsymbol{b_0}\cdot\nabla B_0, \\ \nabla\times\boldsymbol{b}\cdot\nabla\delta\phi = \nabla\times(\boldsymbol{b_0} + \boldsymbol{\delta B_{IS}}/B_0)\cdot\nabla\delta\phi. \end{cases} \tag{4}$$

Equations (2) and (3) can be simplified to

$$\dot{\boldsymbol{R}} = v_\parallel\frac{\boldsymbol{B_0} + \boldsymbol{\delta B_{IS}}}{B_\parallel^*} + \underbrace{\frac{c\left(\boldsymbol{b_0} + \dfrac{\boldsymbol{\delta B_{IS}}}{B_0}\right)\times\nabla\delta\phi}{B_\parallel^*}}_{\boldsymbol{v_E}} + \underbrace{\frac{m_s c}{Z_s B_\parallel^*}v_\parallel^2\nabla\times\boldsymbol{b_0}}_{\boldsymbol{v_c}} + \underbrace{\frac{c\mu}{Z_s B_\parallel^*}\boldsymbol{b_0}\times\nabla B_0}_{\boldsymbol{v_g}}, \tag{5}$$

$$\dot{v_\parallel} = -\frac{1}{m_s}\frac{\boldsymbol{B_0^*} + \boldsymbol{\delta B_{IS}}}{B_\parallel^*}\cdot(\mu\nabla B_0 + Z_s\nabla\delta\phi) - cv_\parallel\frac{\nabla\times\left(\dfrac{\boldsymbol{\delta B_{IS}}}{B_0}\right)}{B_\parallel^*}\cdot\nabla\delta\phi. \tag{6}$$

Here, $\boldsymbol{B_0^*} = \boldsymbol{B_0} + \frac{m_s c}{Z_s}v_\parallel\nabla\times\boldsymbol{b_0}$. The equations of motion (5) and (6) still preserve the Hamiltonian structure[24,25]

$$\nabla\cdot\left(B_\parallel^*\dot{\boldsymbol{R}}\right) + \frac{\partial}{\partial v_\parallel}\left(B_\parallel^*\dot{v_\parallel}\right) = \left\{\begin{array}{l} \dfrac{c\mu}{Z_s}\nabla\cdot(\boldsymbol{b_0}\times\nabla B_0) \\ \quad + c\nabla\cdot\left[\left(\boldsymbol{b_0} + \dfrac{\boldsymbol{\delta B_{IS}}}{B_0}\right)\times\nabla\delta\phi\right] \\ \quad - c\nabla\times\left(\boldsymbol{b_0} + \dfrac{\boldsymbol{\delta B_{IS}}}{B_0}\right)\cdot\nabla\delta\phi \\ \quad - \dfrac{c\mu}{Z_s}\nabla\times\boldsymbol{b_0}\cdot\nabla B_0 \end{array}\right\} = 0. \tag{7}$$

GTC has been developed and successfully tested for both the full-f method and the delta-f method.[26,27] The delta-f method has the advantage of less particle noises over the full-f method. In the delta-f method, both the distribution function f_s and the propagator $\frac{d}{dt}$ are separated into a major equilibrium part and a perturbed part: $\frac{d}{dt} \equiv L_0 + \delta L$ and $f_s = f_{0s} + \delta f_s$. Correspondingly, $\frac{d}{dt} f = Lf = (L_0 + \delta L)(f_{0s} + \delta f_s) = 0$. Applying Eqs. (5) and (6), we can define

$$L_0 = \frac{\partial}{\partial t} - \frac{\mu}{m_s}\frac{\boldsymbol{B}_0^*}{B_{0\|}^*}\cdot\mu\nabla B_0\frac{\partial}{\partial_{v_\|}} + v_\|\frac{\boldsymbol{B_0}}{B_{0\|}^*}\cdot\nabla + \left(\frac{m_s c}{Z_s B_{0\|}^*}v_\|^2\nabla\times\boldsymbol{b_0} + \frac{c\mu}{Z_s B_{0\|}^*}\boldsymbol{b_0}\times\nabla B_0\right)\cdot\nabla, \tag{8}$$

$$\delta L = \left(\frac{B_{0\|}^*}{B_\|^*} - 1\right)L_0 + \left(v_\|\frac{\boldsymbol{\delta B_{IS}}}{B_\|^*} + \frac{c(\boldsymbol{b_0} + \boldsymbol{\delta B_{IS}}/B_0)\times\nabla\delta\phi}{B_\|^*}\right)\cdot\nabla - \frac{1}{m_s}\frac{\boldsymbol{B_0} + \boldsymbol{\delta B_{IS}}}{B_\|^*}\cdot Z_s\nabla\delta\phi\frac{\partial}{\partial_{v_\|}} - \frac{1}{m_s}\frac{\boldsymbol{\delta B_{IS}}}{B_\|^*}\cdot\mu\nabla B_0\frac{\partial}{\partial_{v_\|}} - cv_\|\frac{\nabla\times(\boldsymbol{b_0} + \boldsymbol{\delta B_{IS}}/B_0)}{B_\|^*}\cdot\nabla\delta\phi\frac{\partial}{\partial_{v_\|}}. \tag{9}$$

The equilibrium is defined by $L_0 f_{0s} = 0$ and can be approximated by a local Maxwellian read as

$$f_{0s} = \frac{n_{0s}}{\left(2\pi v_{th,s}^2\right)^{1.5}}\exp\left[-\frac{E_s}{T_{0s}}\right], \tag{10}$$

where $v_{th,s} = \sqrt{T_{0s}/m_s}$ is the thermal speed, E_s is the kinetic energy of the particle, and n_{0s} and T_{0s} are the equilibrium density and temperature, respectively. Inserting $L_0 f_{0s} = 0$ into $Lf_s = 0$ and defining the weight as $w_s = \delta f_s/f_s$, one can use the PIC approach to evolve the system. Defining $\Omega_s = \frac{Z_s B_0}{m_s c}$ as the particle cyclotron frequency, and the operator $\nabla|_{v_\perp} f_{0s} = \left(\nabla + \frac{\mu\nabla B_0}{T_{0s}}\right)f_{0s}$, the dynamic equation for w_s can be expressed as

$$\frac{d}{dt}w_s = -\frac{1}{f_s}\delta L f_{0s} = -(1 - w_s)\times\left[\underbrace{\frac{c(\boldsymbol{B_0} + \boldsymbol{\delta B_{IS}})\times\nabla\delta\phi}{B_0^2}\cdot\frac{1}{f_{0s}}\nabla|_{v_\perp}f_{0s}}_{E\times B} + \underbrace{\frac{v_\|Z_s}{T_{0s}}\left(\frac{\boldsymbol{B_0} + \boldsymbol{\delta B_{IS}}}{B_0}\cdot\nabla\delta\phi\right)}_{parallel} + \underbrace{\frac{Z_s}{T_{0s}}\left(\frac{v_\|^2}{\Omega_s}\nabla\times\boldsymbol{b}_0 + \frac{\mu}{m_s\Omega_s}\boldsymbol{b}_0\times\nabla B_0\right)\cdot\nabla\delta\phi}_{magnetic\ drift} + \underbrace{v_\|\frac{\boldsymbol{\delta B_{IS}}}{B_0}\cdot\frac{1}{f_{0s}}\nabla|_{v_\perp}f_{0s}}_{flatten\ effect}\right]. \tag{11}$$

Here, we use the approximation $B_\|^* = B_{0\|}^* = B_0$ for the dw_s/dt equation, and the island's effect in the magnetic drift terms is also ignored according to the assumption (4).

With Eq. (11) as the basic weight equation, one can use the delta-f method to evolve the plasma system with a static magnetic island. In (11), the $E \times B$ term gives the drive for the ITG instability, the parallel term is the landau damping term, and the last term is the flattening effect of the island. To close the system, the electrostatic potential is solved by the gyrokinetic Poisson equation[28]

$$\frac{Z_i^2 n_{0i}}{T_{0i}}\left(\delta\phi - \delta\tilde{\phi}\right) = Z_i\delta n_i + Z_e\delta n_e. \tag{12}$$

The fluid moments of the particle are calculated by integrating the distribution function over the velocity space. Define the integral operator as $\int d\boldsymbol{v} \equiv \frac{\pi B_0}{m_s}\int dv_\| d\mu$, we have

$$\delta n_s = \int d\boldsymbol{v}\delta f_s. \tag{13}$$

Equations (5), (6), and (8)–(13) form a closed system for gyrokinetic simulation with a static island. The gyroradius of electron ρ_e is small, and for this case, the above model is the drift kinetic electron (DKE) model.

While the hybrid model[29] separately solves the zonal and nonzonal part, the DKE model solves both the zonal and nonzonal components together, which is required in the presence of magnetic islands. We note that using the DKE model for the electrostatic simulation is numerically expensive, where the so-called "ω_H" mode[28] must be resolved. In practice, we use a small simulation time step size and select the modes with small parallel mode numbers to avoid numerical instability.

III. VERIFICATION OF THE SIMULATION MODEL FOR LOW-n MODE GENERATION BY THE MAGNETIC ISLAND

It has been suggested in an early literature[12] that the different responses of ions and electrons to the large magnetic island will excite a strong resonant low-n mode. In this section, we use the DKE model to show that such a low-n mode can be generated in the global kinetic simulation of ITG with an n = 1, m = 2 prescribed island. Note that in the weight equation (11), the simulation model of the magnetic island will cause large perturbations that directly lead the system into the nonlinear stage. To show the low-n mode generation and its transition from the linear stage into the nonlinear stage, we turn off the flattened effect [i.e., the last term of Eq. (11) is neglected] in this section.

Simulation parameters in this paper are as follows: the inversed aspect ratio $a/R_0 = 0.42$, where a is the minor radius and R_0 is the major radius, the ion gyroradius $\rho_i/R_0 = 2.86 \times 10^{-3}$. At the magnetic axis, $T_e = T_i = 2.22\,\mathrm{keV}$, $n_e = n_i = 1.13 \times 10^{13}\,\mathrm{cm}^{-3}$, $B_0 = 20125\,\mathrm{G}$. At the diagnostic surface, $r = 0.5a$, $q = 2$, and the magnetic shear $\hat{s} = 0.54$. The characteristic lengths of the density and temperature gradients are defined as $L_n = \frac{n_0}{dn_0/dr}$, $L_T = \frac{T_0}{dT_0/dr}$. At $r = 0.5a$, $R_0/L_{ni} = R_0/L_{ne} = 1.9$, $R_0/L_{Ti} = R_0/L_{Te} = 6.0$. We use 100 grid points in the radial direction and 400 in the poloidal direction to make the grid size nearly equal in the radial and poloidal directions ($r\Delta\theta \approx \Delta r \approx \rho_i$). For the parallel direction, 32 points are used. The particles per cell are 100 for both the electrons and ions. We only keep 5 toroidal modes in all simulations: the (n = 0, m = 0) mode, the (n = 1, m = 2) harmonic for the long wavelength fluctuation that is related to the island and

three high-n modes ($n=9$, 10, 11, $m=10\sim30$) that are dominated by the ITG.

The n = 1, m = 2 magnetic island is introduced in the simulation by adding an external parallel vector potential $\delta A_{\parallel}^{IS} = -A_{\parallel 0}R_0B_0\cos(2\theta-\zeta)\times h(r-r_0)$ to the equilibrium magnetic field and $\boldsymbol{\delta B_{IS}} = \nabla\times(\delta A_{\parallel}^{IS}\boldsymbol{b}_0)$. We use $A_{\parallel 0}=0.0001$ and $r_0=0.5a$. Here, $h(r-r_0)$ is a radial envelope function used to suppress $\delta A_{\parallel}^{IS}$ at the simulation boundary, expressed as

$$h(r-r_0)=\left(1+\tanh\frac{2(r-r0)}{r_0}\right)\left(1+\tanh\frac{2(r_0-r)}{r_0}\right). \quad (14)$$

By defining the equilibrium magnetic shear as $\hat{s}=\frac{r}{q}\frac{dq}{dr}$, the width of the magnetic island is estimated by

$$W=\sqrt{\frac{8qA_{\parallel 0}R_0}{B_0\hat{s}}}. \quad (15)$$

For our case, the calculated magnetic island width is $W=0.13a=22\rho_i$. The island's helical field line structure is represented with the magnetic helical flux function defined as

$$\psi_{he}=\psi_0-\frac{\psi_{0t}}{2}-\frac{\delta A_{\parallel}^{IS}}{B_0}g, \quad (16)$$

where ψ_0 and ψ_{0t} are the magnetic poloidal flux function and the toroidal flux function and g is defined through the covariant representation of the equilibrium magnetic field $\boldsymbol{B_0}=I\nabla\theta+g\nabla\zeta$.

We first compare the DKE model described in Sec. II with the hybrid model[30] for the ITG simulation when the magnetic island is not applied, and the details are not shown here. The results show that the two models agree well for the same ITG mode real frequency and the nonlinear saturation level, but the linear growth rate is 18% higher in the DKE model. We would like to emphasize that in this paper, we aim to study the nonlinear effects of the magnetic island on the ITG turbulence. We think that the differences in the linear ITG growth rate should not affect qualitatively the nonlinear results (i.e., the magnetic island can induce vortex mode and helical shear flow to suppress ITG turbulence). The discrepancy in the ITG growth rates between the electrostatic hybrid model[30] and the DKE model is being investigated and will be reported in a future publication.

Next, to show the island's effect of generating the low-n mode, we use the DKE model to carry out two simulations for comparison, one with the prescribed (1,2) magnetic island and the other not. We normalize the electrostatic potential as $\frac{e\delta\phi}{T_e}$ and trace the time histories of the (n = 10, m = 20) ITG mode $\delta\phi^{10,20}$ and the (n = 1, m = 2) mode $\delta\phi^{1,2}$ at the diagnostic point ($\theta=0$, $r=0.5a$). The (n = 0, m = 0) mode is averaged over the simulation domain as $\langle\delta\phi^{0,0}\rangle$. The results are shown in Fig. 1. First, for the case without the island (red lines), in the linear stage starting from $t=10R_0/C_s$ to $t=20R_0/C_s$, the ITG component $\delta\phi^{10,20}$ grows linearly with a growth rate of $\gamma^{10,20}\sim0.55C_s/R_0$ and the real frequency of $\omega^{10,20}\sim0.41C_s/R_0$. $\delta\phi^{1,2}$ and $\langle\delta\phi^{0,0}\rangle$ in this stage are mostly numerical noises, i.e., small amplitudes with a growth rate close to that of ITG. Starting from $t=20R_0/C_s$, $\langle\delta\phi^{0,0}\rangle$ grows rapidly with a growth rate of $\gamma^{0,0}\sim2\gamma^{10,20}$. After $t=26R_0/C_s$, the system saturates nonlinearly, and the amplitude of the n = 0 field is of two orders of magnitude larger than that of the dominant mode $\delta\phi^{10,20}$ and $\delta\phi^{1,2}$.

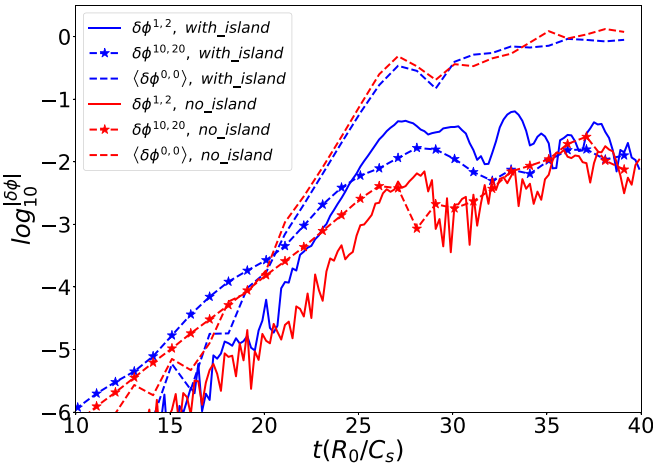

FIG. 1. The time history of the n = 1, m = 2 component of the electrostatic potential (solid), the n = 10, m = 20 dominant ITG mode (star), and the volume averaged n = 0, m = 0 mode (dashed). The case with the island is colored in blue, and the case without the island is colored in red.

There are some differences when the magnetic island is applied (blue lines). At the transition stage $t=20R_0/C_s$ to $t=26R_0/C_s$, the amplitude of $\delta\phi^{1,2}$ is substantially larger than that of the no island case. This indicates that $\delta\phi^{1,2}$ resonates with the n = 1, m = = 2 magnetic island. At the nonlinear stage after $t=26R_0/C_s$ to $t=35R_0/C_s$, $\delta\phi^{1,2}$ is found to have a saturation level much larger than that of the no island case.

To further demonstrate the resonant process of the low-n mode with the magnetic island, we draw the poloidal contour plot for $\delta\phi^{1,2}$ and $\delta\phi^{n>1}$ in the nonlinear stage at $t=30R_0/C_s$. Here, $\delta\phi^{n>1}=\delta\phi-\delta\phi^{0,0}-\delta\phi^{1,2}$ is the high n components of the ITG electrostatic potential. In Fig. 2(a), a large scale $\delta\phi^{1,2}$ structure resonating with the magnetic island is observed, which is absent in the no island case Fig. 2(c). For the high-n ITG components $\delta\phi^{n>1}$, the mode structure is slightly modified by the magnetic island. In Fig. 2(b), the mode is stronger near the island separatrix, while in Fig. 2(d), the ITG structure shows a typical structure that is regulated by the zonal flow.

IV. EFFECTS OF THE MAGNETIC ISLAND ON ITG TURBULENCE

To investigate the full effects of the magnetic island on the ITG instability, we keep the flattening effect in the system for the simulations in this section using the same parameters. First, we turn off the electrostatic potential $\delta\phi$ and keep the magnetic island as the only perturbation to run the system for $20R_0/C_s$ until it attains a flattened state. In Fig. 3(a), the red solid line shows the radial ion density profile at $t=20R_0/C_s$ which is flattened within the island region on the high field side ($\theta=\pi$). In Fig. 3(b), the time history of the ion density gradient at the island O-point ($\zeta=0$, $\theta=\pi$, $r=0.5a$) is shown to decrease gradually to zero in the flatten process. After the flattened state is built, we use it as the initial perturbation for the system and turn on the electrostatic field $\delta\phi$ for self-consistent simulation. Note that the initial perturbation is large due to the flattened ion density, and we enforce charge neutrality by initiating the electron distribution function with $\delta f_e=\delta f_i$ at $t=20R_0/C_s$ and let the system run freely.

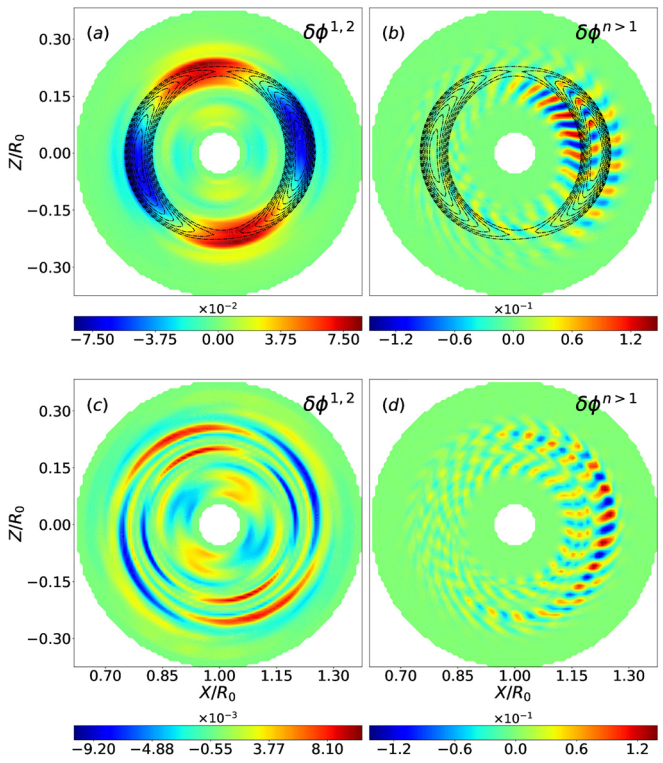

FIG. 2. Poloidal contour plots at $t = 30R_0/C_s$ of the n = 1, m = 2 mode [(a) and (c)] and the $n > 1$ components of the ITG dominant mode [(b) and (d)] for the case with the island (upper) and the case without the island (lower). The magnetic island structure is illustrated with the black dashed lines.

The simulation with the relaxed profiles finds that the n = 1, m = 2 mode can be well sustained in the nonlinear stage, and more interestingly, couples to the n = 0, m = 0 mode with the geodesic acoustic mode (GAM)[22,23] frequency. In Fig. 4, the time histories of the real part of $\delta\phi^{1,2}$, $\delta\phi^{0,0}$ and the dominant ITG modes $\delta\phi$[9–11,18–20] at the diagnostic point ($r = 0.5a$) are shown. It is clear that $\delta\phi^{1,2}$ (blue line) and $\delta\phi^{0,0}$ (purple line) synchronously oscillate with an estimated frequency of $\omega = 2.09C_s/R_0$, which is close to the theoretical GAM

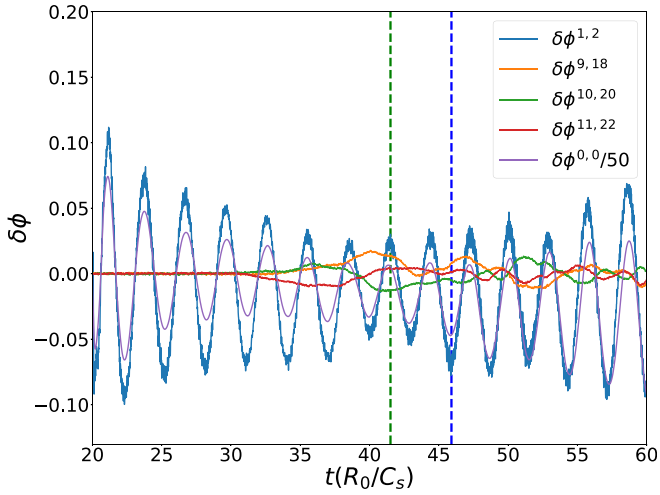

FIG. 4. The time history of different toroidal modes in the self-consistent simulation with the magnetic island. The n = 1, m = 2 electrostatic mode (blue solid) and the n = 0, m = 0 mode (purple solid) oscillate synchronously with a frequency of $2.09C_s/R_0$, and $\delta\phi^{0,0}$ is divided by 50 for comparison.

frequency $\omega_{GAM} \approx \sqrt{2(7/4+1)}C_s/R_0$. We would like to emphasize that this synchronization of GAM and magnetic islands has recently been observed in a HL-2A experiment.[31] To further show the island flattening effect's influence on the electrostatic modes, we plot the $\delta\phi^{1,2}$ and the $\delta\phi^{n>1}$ poloidal mode structures at $t = 41.5R_0/C_s$ (green dashed line in Fig. 4) and at $t = 46R_0/C_s$ (blue dashed line in Fig. 4). $\delta\phi^{1,2}$ is found to highly resonant with the magnetic island, see Figs. 5(a) and 5(b). For $\delta\phi^{n>1}$, we observe a significant change in the ITG mode structure, which is suppressed at the magnetic island's O-point and strengthened around the X-point, as shown in Figs. 5(c) and 5(d).

It has been experimentally and numerically pointed out that the large magnetic island can generate strong shear flow around it, which substantially suppress the local turbulence and play an important role in the formation of the internal transport barrier (ITB).[6,15,32] Indeed, in our simulation, we observe that the vortex mode ($\delta\phi^{1,2}$) can generate clear helical shear flow around the magnetic island. We define the helical flow as

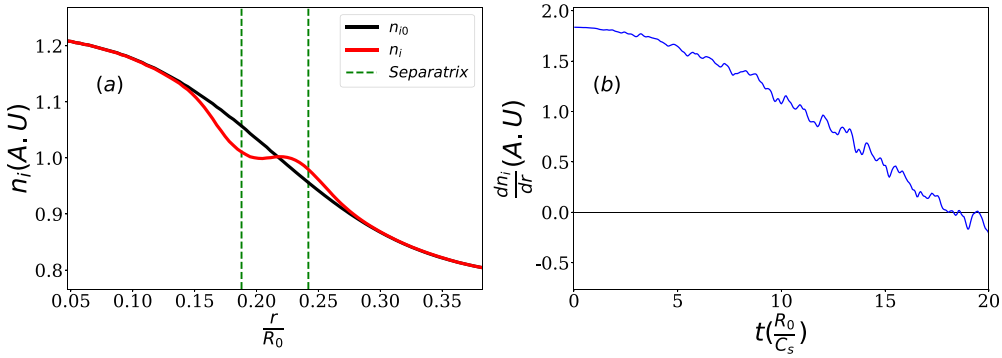

FIG. 3. (a) The ion density profiles for the equilibrium (black solid line) and the flattened state (red solid line) on the high field side ($\theta = \pi$). (b) The time history of the ion density gradient $\frac{dn_i}{dr}$ at the O-point on the high field side ($\theta = \pi$, $r = 0.5a$) during the flattening process.

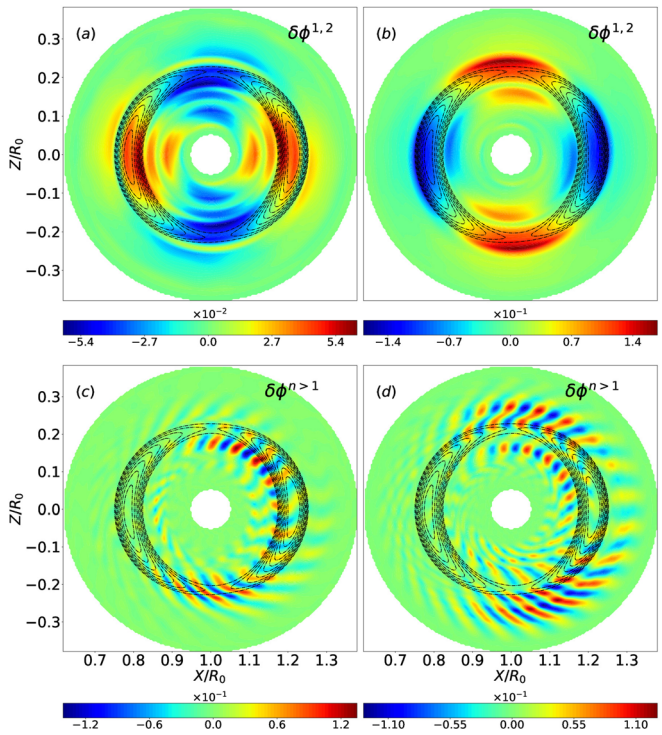

FIG. 5. The electrostatic modes structures in the presence of magnetic island flattening effects: the upper two panels [(a) and (b)] show the n = 1, m = 2 mode poloidal structures at $t = 41.5R_0/C_s$ and $t = 46R_0/C_s$. The $n > 1$ components of the ITG mode structures are shown in (c) and (d).

$$\xi = m\theta - n\zeta, \tag{17}$$

$$v_\xi = -\frac{\nabla\delta\phi^{n>0} \times \boldsymbol{B}}{B_0^2} \cdot \boldsymbol{e}_\xi. \tag{18}$$

Here, ξ is the helical angle and n, m = 1, 2 and $\delta\phi^{n>0}$ is the electrostatic potential without the n = 0 part. We calculate the time averaged helical flow $\langle v_\xi \rangle_t$ in the time range of $t \in [35, 45]\ R_0/C_s$. In Fig. 6(a), we plot the radial profile of the helical flow across the island O-point at the weak field side ($\theta = 0$), and it is clear that near the island separatrix the helical flow has a strong shear structure. We also plot the poloidal structure of $\langle v_\xi \rangle_t$ in Fig. 6(b), and substantial helical shear flow is observed at the island separatrix. Note that in Figs. 5(c) and 5(d), the ITG mode structure is weak at the separatrix, and this can be explained by the helical flow shearing effect, which suppress the ITG mode significantly. We would like to emphasize that our work verifies the existence of the helical shear flow in the global particle nonlinear simulation, and this can be an important reference to explain the experiment observations.[32]

We now examine the magnetic island's effect on the ITG turbulence and transport. Compared with the no-island case, we find that the island tends to suppress the turbulence intensity inside the island region and shifts the transport mainly toward the X-point. To clarify this, we compare the ion density fluctuations in the nonlinear stage for both the cases with and without the island, which are averaged over the nonlinear stage ranges from $t = 30R_0/C_s$ to $t = 40R_0/C_s$ in Fig. 1 for the no-island case and $t = 45R_0/C_s$ to $t = 55R_0/C_s$ in Fig. 4 for the island case. The turbulence intensity can be represented by the ion density variance $\tilde{n}_i^2(\boldsymbol{r})$ calculated as

$$\tilde{n}_i^2(\boldsymbol{r}) = \langle \left[n_i(\boldsymbol{r}, t) - \langle n_i(\boldsymbol{r}, t) \rangle_t \right]^2 \rangle_t . \tag{19}$$

We use $\tilde{n}_i^2(\boldsymbol{r})$ to label the ion turbulence intensity in the no-island case and $\tilde{n}_i'^2(\boldsymbol{r})$ in the island case and measure their difference as

$$\Delta\tilde{n}_i^2(\boldsymbol{r}) = \tilde{n}_i'^2(\boldsymbol{r}) - \tilde{n}_i(\boldsymbol{r}). \tag{20}$$

Figure 7(a) shows the poloidal contour of $\Delta\tilde{n}_i^2(\boldsymbol{r})$ normalized to the volume averaged value $\langle \tilde{n}_i^2(\boldsymbol{r}) \rangle$ of the no island case. It is clear that the ion density turbulence is decreased around the O-point region but is strengthened near the X-point and outside the island. We find that the regulation effect of the island on the transport is also prominent. We

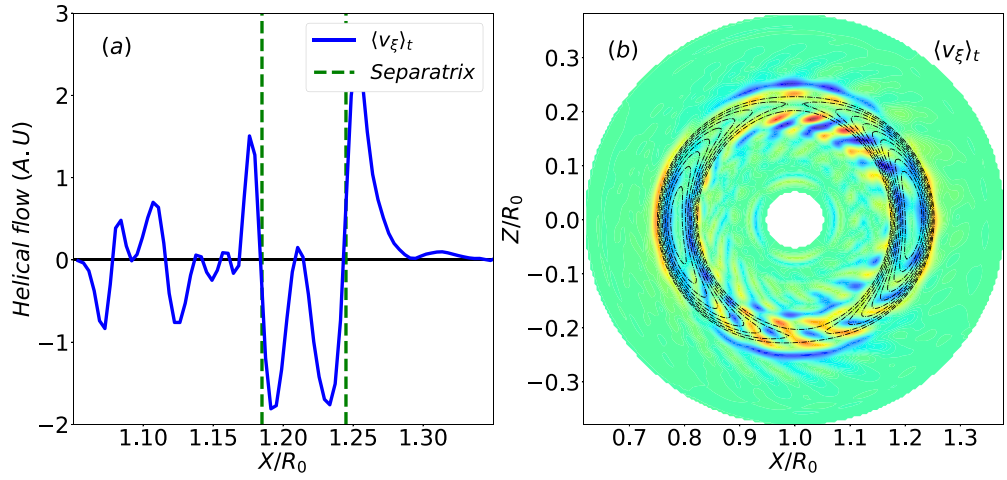

FIG. 6. The time averaged helical shear flow induced by the magnetic island. (a) the radial profile of the helical shear flow across the O-point at the weak field side ($\theta = 0$, $\zeta = 0$) and (b) the poloidal plot of the helical shear flow.

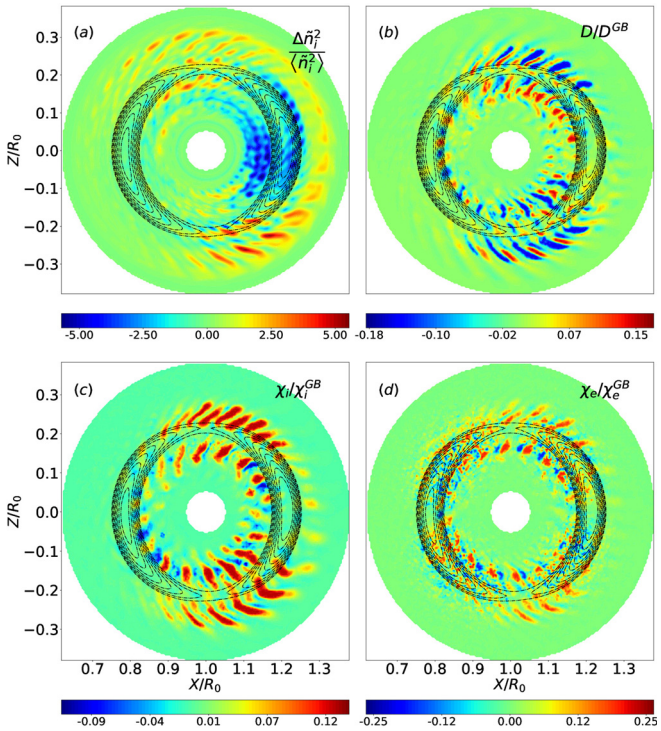

FIG. 7. The poloidal contour plots of the difference in fluctuations and transport from the simulations with and without the island. (a) ion density fluctuation intensity; (b) the particle diffusivity; (c) the ion heat conductivity; and (d) the electron heat conductivity.

demonstrate this by measuring the particle diffusivities and the heat conductivities in the nonlinear stage. Defining the particle diffusivity and the heat conductivity (e.g., for ion) as $D = \frac{1}{n_{0i}\nabla n_{0i}}\int dv v_r \delta f_i$ and $\chi_i = \frac{1}{n_{0i}\nabla T_{0i}}\int dv\left(\frac{1}{2}m_i v^2 - \frac{3}{2}T_i\right)v_r\delta f_i$, where v_r is the total radial velocity consisting of the $E\times B$ drift and magnetic island induced flutter motion. The gyro-Bohm units $D^{GB} = \chi_i^{GB} = \rho_i^2 v_i/a$ are used for normalization, where $v_i = \sqrt{T_i/m_i}$ and $\rho_i = v_i m_i c/eB_0$. In Figs. 7(b)–7(d), we show the poloidal contour plots of the two species' particle and heat transport levels in the island case at the nonlinear stage $t = 45R_0/C_s$. First, the ion particle flux [Fig. 7(b)] and the heat flux [Fig. 7(c)] peak near the island X-point, which is consistent with the modified ITG mode structure that is suppressed around the O-point. The electron heat transport also exhibits the same pattern [Fig. 7(d)]. Note that the total radial velocity v_r has the component of the magnetic island flutter motion, which is much bigger for the electron due to the small particle mass. Consequently, for the electron, there are some noisy values observed, especially at the strong field side where the ITG mode is weak.

V. CONCLUSION

In this work, we have formulated and then implemented an electrostatic model in GTC to study the nonlinear effect of the n = 1, m = 2 magnetic island on the ITG instability. Gyrokinetic ions and drift-kinetic electrons are used to accurately keep the particles' kinetic effects. In our simulation, first we demonstrate an n = 1, m = 2 electrostatic mode that can be generated by the magnetic island with the same vortex structure of the island. In the simulation with the magnetic flattening effect, the plasma profiles are greatly flattened in the island region. Based on these relaxed profiles, self-consistent simulation finds that the n = 1, m = 2 vortex mode can be well preserved and, interestingly, couples to the n = 0, m = 0 mode to synchronously oscillate with the GAM frequency. The magnetic island also has a substantial influence on the ITG mode. We find the nonlinear ITG structure is highly modified by the island, which is strengthened near the X-point and suppressed at the O-point. We also find that the magnetic island can regulate the ITG turbulence and transport, simulation shows that the turbulence is substantially diminished in the island region, and the ion and electron particle and heat fluxes are localized near the X-point. Finally, we have observed a clear helical shear flow induced by the magnetic island, which suppresses the turbulence at the island separatrix and can be a transport barrier that has been pointed out in the experiments.[32]

ACKNOWLEDGMENTS

The author is thankful for useful discussions with J. Bao, P. F. Liu, L. Shi, and GTC Team. This work was supported by the China National Magnetic Confinement Fusion Science Program (Grant No. 2018YFE0304100), the U.S. Department of Energy (DOE) SciDAC ISEP Program, and the China Scholarship Council (Grant No. 201306010032). This work used resources of the Oak Ridge Leadership Computing Facility at the Oak Ridge National Laboratory (DOE Contract No. DE-AC05-00OR22725) and the National Energy Research Scientific Computing Center (DOE Contract No. DE-AC02-05CH11231).

REFERENCES

[1]R. Nazikian, C. Paz-Soldan, J. D. Callen, D. Eldon, T. Evans, N. Ferraro, B. Grierson, R. Groebner, S. Haskey, C. Hegna *et al.*, "Pedestal bifurcation and resonant field penetration at the threshold of edge-localized mode suppression in the DIII-D tokamak," Phys. Rev. Lett. **114**(10), 105002 (2015).
[2]M. Choi, J. Kim, J.-M. Kwon, H. Park, Y. In, W. Lee, K. Lee, G. Yun, J. Lee, M. Kim *et al.*, "Multiscale interaction between a large scale magnetic island and small scale turbulence," Nucl. Fusion **57**(12), 126058 (2017).
[3]T. Hender, J. Wesley, J. Bialek, A. Bondeson, A. Boozer, R. Buttery, A. Garofalo, T. Goodman, R. Granetz, Y. Gribov *et al.*, "MHD stability, operational limits and disruptions," Nucl. Fusion **47**(6), S128 (2007).
[4]W. W. Heidbrink, L. Bardoczi, C. S. Collins, G. J. Kramer, R. J. La Haye, D. Lin, C. M. Muscatello, M. Podesta, L. Stagner, M. A. Van Zeeland *et al.*, "The phase-space dependence of fast-ion interaction with tearing modes," Nucl. Fusion **58**(8), 082027 (2018).
[5]G. Dong and Z. Lin, "Effects of magnetic islands on bootstrap current in toroidal plasmas," Nucl. Fusion **57**(3), 036009 (2017).
[6]J. Connor, T. Fukuda, X. Garbet, C. Gormezano, V. Mukhovatov, M. Wakatani *et al.*, "A review of internal transport barrier physics for steady-state operation of tokamaks," Nucl. Fusion **44**(4), R1 (2004).
[7]H. Wilson and J. Connor, "The influence of magnetic islands on drift mode stability in magnetized plasma," Plasma Phys. Controlled Fusion **51**(11), 115007 (2009).
[8]P. Jiang, Z. Lin, I. Holod, and C. Xiao, "Effects of magnetic islands on drift wave instability," Phys. Plasmas **21**(12), 122513 (2014).
[9]Z. Wang, J. Li, Y. Kishimoto, and J. Dong, "Magnetic-island-induced ion temperature gradient mode," Phys. Plasmas **16**(6), 060703 (2009).
[10]Z. Hu, Z. Wang, L. Wei, J. Li, and Y. Kishimoto, "Nonlinear mutual destabilization of the tearing mode and ion temperature gradient mode," Nucl. Fusion **54**(12), 123018 (2014).

[11]W. Wei, W. Zhengxiong, L. Jiquan, Y. Kishimoto, D. Jiaqi, and S. Zheng, "Magnetic-island-induced ion temperature gradient mode: Landau damping, equilibrium magnetic shear and pressure flattening effects," Plasma Sci. Technol. **20**(7), 075101 (2018).
[12]W. Hornsby, A. Peeters, E. Poli, M. Siccinio, A. Snodin, F. J. Casson, Y. Camenen, and G. Szepesi, "On the nonlinear coupling between micro turbulence and mesoscale magnetic islands in a plasma," Europhys. Lett. **91**(4), 45001 (2010).
[13]W. Hornsby, A. Peeters, M. Siccinio, and E. Poli, "On the dynamics of vortex modes within magnetic islands," Phys. Plasmas **19**(3), 032308 (2012).
[14]A. Ishizawa and N. Nakajima, "Thermal transport due to turbulence including magnetic fluctuation in externally heated plasma," Nucl. Fusion **49**(5), 055015 (2009).
[15]J.-M. Kwon, S. Ku, M. Choi, C. Chang, R. Hager, E. Yoon, H. Lee, and H. Kim, "Gyrokinetic simulation study of magnetic island effects on neoclassical physics and micro-instabilities in a realistic KSTAR plasma," Phys. Plasmas **25**(5), 052506 (2018).
[16]A. B. Navarro, L. Bardóczi, T. Carter, F. Jenko, and T. Rhodes, "Effect of magnetic islands on profiles, flows, turbulence and transport in nonlinear gyrokinetic simulations," Plasma Phys. Controlled Fusion **59**(3), 034004 (2017).
[17]W. M. Tang, "Microinstability theory in tokamaks," Nucl. Fusion **18**(8), 1089 (1978).
[18]W. Horton, "Drift waves and transport," Rev. Mod. Phys. **71**(3), 735 (1999).
[19]Z. Lin, T. S. Hahm, W. Lee, W. M. Tang, and R. B. White, "Turbulent transport reduction by zonal flows: Massively parallel simulations," Science **281**(5384), 1835–1837 (1998).
[20]W. Deng, Z. Lin, and I. Holod, "Gyrokinetic simulation model for kinetic magnetohydrodynamic processes in magnetized plasmas," Nucl. Fusion **52**(2), 023005 (2012).
[21]S. Nishimura, S. Benkadda, M. Yagi, S.-I. Itoh, and K. Itoh, "Nonlinear dynamics of rotating drift-tearing modes in tokamak plasmas," Phys. Plasmas **15**(9), 092506 (2008).
[22]N. Winsor, J. L. Johnson, and J. M. Dawson, "Geodesic acoustic waves in hydromagnetic systems," Phys. Fluids **11**(11), 2448–2450 (1968).
[23]K. Zhao, T. Lan, J. Dong, L. Yan, W. Hong, C. Yu, A. Liu, J. Qian, J. Cheng, D. Yu *et al.*, "Toroidal symmetry of the geodesic acoustic mode zonal flow in a tokamak plasma," Phys. Rev. Lett. **96**(25), 255004 (2006).
[24]T. Hahm, "Nonlinear gyrokinetic equations for tokamak microturbulence," Phys. Fluids **31**(9), 2670–2673 (1988).
[25]A. Brizard and T. Hahm, "Foundations of nonlinear gyrokinetic theory," Rev. Mod. Phys. **79**(2), 421 (2007).
[26]S. Parker and W. Lee, "A fully nonlinear characteristic method for gyrokinetic simulation," Phys. Fluids B **5**(1), 77–86 (1993).
[27]G. Hu and J. A. Krommes, "Generalized weighting scheme for δ f particle-simulation method," Phys. Plasmas **1**(4), 863–874 (1994).
[28]W. Lee, "Gyrokinetic particle simulation model," J. Comput. Phys. **72**(1), 243–269 (1987).
[29]I. Holod, W. Zhang, Y. Xiao, and Z. Lin, "Electromagnetic formulation of global gyrokinetic particle simulation in toroidal geometry," Phys. Plasmas **16**(12), 122307 (2009).
[30]Z. Lin, Y. Nishimura, Y. Xiao, I. Holod, W. Zhang, and L. Chen, "Global gyrokinetic particle simulations with kinetic electrons," Plasma Phys. Controlled Fusion **49**(12B), B163 (2007).
[31]K. Zhao, Y. Nagashima, P. Diamond, J. Dong, K. Itoh, S.-I. Itoh, L. Yan, J. Cheng, A. Fujisawa, S. Inagaki *et al.*, "Synchronization of geodesic acoustic modes and magnetic fluctuations in toroidal plasmas," Phys. Rev. Lett. **117**(14), 145002 (2016).
[32]K. Ida and T. Fujita, "Internal transport barrier in tokamak and helical plasmas," Plasma Phys. Controlled Fusion **60**(3), 033001 (2018).